Research Article

Journal of Environmental Nanotechnology

Construction of Double S-scheme $CaWO_4/g\text{-}C_3N_4/WO_3$ Ternary Heterojunction for Efficient Photocatalytic Degradation of Rhodamine B

A. Vadivu[1], M. Venkatachalam[2*], K. Sampath[3], M. Nagoor Meeran[4] and Paulraj Arunkumar[5]

[1]Department of Chemistry, Periyar University, Salem, TN, India
[2]Department of Chemistry, Government Arts College for Men, Krishnagiri, TN, India
[3]Department of Chemistry, Kumaraguru College of Technology, Coimbatore, TN, India
[4]Department of Chemistry, Vel Tech Rangarajan Dr. Sagunthala R&D Institute of Science and Technology, Avadi, Chennai, TN, India
[5]School of Chemical Engineering, Optoelectronic Convergence Research Center, Chonnam National University, Buk-gu, Gwangju, Gyeonggi Province, Republic of Korea

Received: 02.03.2026 Accepted: 11.03.2026 Published: 30.03.2026

*venkatphd06@gmail.com

ABSTRACT

$CaWO_4/g\text{-}C_3N_4/WO_3$ ternary nanocomposites were synthesized via a hydrothermal method, followed by ultrasonic-assisted composite formation. The structural, optical, and morphological properties of the nanocomposites were systematically characterized using X-ray diffraction (XRD), ultraviolet–visible diffuse reflectance spectroscopy (UV–DRS), photoluminescence (PL), Fourier-transform infrared spectroscopy (FTIR), field-emission scanning electron microscopy (FESEM), transmission electron microscopy (TEM), and X-ray photoelectron spectroscopy (XPS). XRD analysis confirms the coexistence of calcium tungstate ($CaWO_4$), graphitic carbon nitride ($g\text{-}C_3N_4$), and tungsten trioxide (WO_3) in the ternary nanocomposites, and the shift in the diffraction pattern suggests the presence of interfacial interaction among the components. Optical absorption studies exhibit a distinct red shift with increasing WO_3 content, and a reduction in the band gap is evidenced from the Tauc plot. Among all the compositions, TC5 exhibited the best photocatalytic performance, degrading 98% of Rhodamine B (RhB) in 75 min. The enhanced performance was attributed to optimized charge separation and the formation of a robust double S-scheme heterojunction. The key role of HO• and O_2^{-}• species in the photodegradation of RhB was identified by radical trapping experiments. In summary, at the optimum concentration, the synergy among the scheelite $CaWO_4$ crystalline framework, π-conjugated $g\text{-}C_3N_4$, and defect-rich WO_3 enhances charge separation via a double S-scheme mechanism, enabling rapid ROS generation and making TC5 superior among the synthesized photocatalysts.

Keywords: Ternary nanocomposites; Photocatalytic degradation; Double S-scheme heterojunction; Ultrasonic-assisted synthesis; Radical trapping experiments; Wastewater treatment.

1. INTRODUCTION

The intensified industrial activity and human interventions have created a significant impact on water bodies and the aquatic environment owing to the discharge of hazardous organics via industrial as well as domestic effluents (Singh *et al.* 2023). At present, coagulation, adsorption, filtration, and chemical oxidation are employed to treat polluted water (Kato and Kansha, 2024). However, these technologies exhibit limited degradation efficiency, secondary pollutant generation, and high operational cost, restricting their long-term sustainability (Feijoo *et al.* 2023; Matesun *et al.* 2024). Conversely, semiconductor photocatalysis emerges as a promising eco-friendly alternative, capable of mineralizing a wide range of pollutants into non-toxic byproducts like CO_2 and H_2O under mild conditions (Jabbar *et al.* 2024; Shobana *et al.* 2024).

Photocatalysis is fundamentally based on light-induced excitation of semiconductors, which generates charge carriers that facilitate the redox reactions at the semiconductor surface (Mohamadpour and Amani, 2024). However, most single-component photocatalysts face limitations such as wide band gaps that restrict visible light utilization, rapid charge carrier recombination, low surface activity, and poor catalytic stability (Li *et al.* 2022a). These limitations have prompted researchers to develop multi-component photocatalysts with improved light absorption, efficient charge separation, and tailored band structures.

Nanocomposite photocatalysts have received considerable attention owing to their ability to synergize the properties and advantages of individual semiconductors. A cautious selection of nanocomposite components, based on their band structure, charge transfer characteristics, and chemical reactivity, is essential for designing efficient nanocomposite photocatalysts (Gumma *et al.* 2024). Calcium tungstate ($CaWO_4$), a scheelite-type oxide, is recognized for its

robust structural stability, chemical resilience, and excellent luminescence properties (Yi and Jung, 2021). Despite these advantages, $CaWO_4$ is incapable of absorbing visible light owing to its wide band gap (3.7 eV), which limits its photocatalytic activity (Maurera *et al.* 2004).

Conversely, graphitic carbon nitride (g-C_3N_4) exhibits a narrow band gap (2.7 eV) with other advantages such as a layered structure, high thermal and chemical stability, facile synthesis, tunable band structure, and strong reduction ability (Singhal *et al.* 2024). Nevertheless, its photocatalytic performance is hindered by its rapid charge carrier recombination, low carrier mobility, and poor conductivity (Balakrishnan and Chinthala, 2022).

Tungsten trioxide (WO_3) exhibits a comparatively narrow bandgap (2.6 eV) and supports this photocatalytic system owing to its strong oxidative potential, visible light absorption, and good photostability (Murillo-Sierra *et al.* 2021). However, its conduction band is positioned too positively, which hinders its electron mobility (Dutta *et al.* 2021; Samuel *et al.* 2022). Therefore, combining $CaWO_4$, g-C_3N_4, and WO_3 is expected to integrate their advantages, enabling improved charge and enhanced visible light photocatalytic activity.

Although conventional heterojunctions improve charge separation, the migration of charge carriers to less reactive band positions often reduces the redox ability of the photocatalyst. The proposed system is expected to promote interfacial charge transfer and extend visible-light absorption via the formation of a double S-scheme heterojunction. This heterojunction allows the recombination of energetically undesirable charge carriers while preserving the reactive ones at their corresponding band edges, resulting in improved separation and migration of photogenerated charge carriers, stronger redox capabilities, and increased reactive oxygen species generation (ROS), which are key factors for efficient photocatalytic degradation.

Vadivu *et al.* (2025) developed a binary nanocomposite, $CaWO_4$/g.C_3N_4, with varying compositions and evaluated the photocatalytic degradation performance towards RhB under visible light. Among several compositions, the nanocomposite containing 3 wt.% g-C_3N_4 (denoted as CC3) demonstrated the highest photocatalytic degradation efficiency against Rhodamine B (98% in 150 min under visible light). This remarkable performance is ascribed to enhanced charge separation and improved light absorption. Furthermore, CC3 showed excellent structural stability and recyclability, making it a suitable candidate for developing ternary photocatalysts.

Motivated by the performance of binary nanocomposite (CC3), this study aims to design and develop $CaWO_4$/g-C_3N_4/WO_3 ternary systems with a double S-scheme heterojunction architecture. The incorporation of WO_3 is expected to improve the charge separation efficiency, optimize the band alignment, and broaden the visible-light absorption of nanocomposites via the formation of a double S-scheme heterojunction. The ultimate objective of this approach is to construct a stable visible-light-active photocatalyst for the degradation of organic pollutants.

2. MATERIALS

The chemicals used in the present work were purchased from Loba Chemie, Mumbai, India, including calcium nitrate tetrahydrate ($Ca(NO_3)_2{\cdot}4H_2O$, 98%), sodium tungstate ($Na_2WO_4{\cdot}2H_2O$, 98%), hydrochloric acid (HCl, 35%), and melamine ($C_3H_6N_6$, extra pure), while Rhodamine B ($C_{28}H_{31}ClN_2O_3$, 98%) was purchased from HiMedia, Mumbai, India. All the chemicals were used without further purification.

2.1 Experimental Methods

2.1.1 Synthesis of $CaWO_4$ Nanostructures

The $CaWO_4$ nanostructures were synthesized as per our previous report (Vadivu *et al.* 2025). Equimolar ratio of Ca $(NO_3)_2.4H_2O$ and $Na_2WO_4.2H_2O$ was taken and dissolved separately in 30 mL of deionized water, and mixed with vigorous stirring for 30 min. The contents were then transferred to a 100 mL autoclave and heated at 180 °C for 8 h. After cooling to room temperature, the precipitates were collected by centrifugation, washed thrice with deionized water and ethanol. The precipitates were dried at 80 °C to obtain $CaWO_4$ nanostructures, labelled as CW.

2.1.2 Preparation of g-C_3N_4 Nanostructures

g-C_3N_4 nanostructures were prepared following the reported literature (Niu *et al.* 2012). 5 g of melamine was taken in an alumina crucible and covered with the lid. The melamine was heated at 550 °C for 4 h, and the contents were allowed to cool naturally. The resulting yellow solid g-C_3N_4 (labelled as CN) was powdered using a mortar and pestle.

2.1.3 Preparation of WO_3 Nanostructures

WO_3 is synthesized with slight modifications based on the reported literature (Tahir *et al.* 2018). In this modified synthesis procedure, 10 mmol of $Na_2WO_4.2H_2O$ was dissolved in 60 mL of water, and then 1:1 HCl was added dropwise under vigorous stirring until a yellow precipitate was obtained. The contents were transferred into a Teflon-lined autoclave and then heated at 180 °C for 24 h. After cooling to room temperature, the contents were centrifuged, washed repeatedly with water and ethanol. The obtained

precipitate was dried at 80 °C to yield a yellow powder of WO_3 nanostructures.

2.1.4 Synthesis of Ternary Nanocomposites

Table 1. Weights of CC3 and WO_3 used in the preparation of $CaWO_4$/g-C_3N_4/WO_3 ternary nanocomposites

S. No.	Weight of CC3 (mg)	Weight of WO_3 (mg)	Ternary Nanocomposites
1	495	5	TC1
2	485	15	TC3
3	475	25	TC5
4	465	35	TC7
5	455	45	TC9

The nanocomposites were prepared by ultrasonication of the calculated quantities of pre-synthesized nanostructures. $CaWO_4$/g-C_3N_4 binary nanocomposites were prepared as reported earlier (Vadivu *et al*. 2025) by ultrasonication of 97 wt.% $CaWO_4$ and 3 wt.% g-C_3N_4 in water, followed by separation, washing with ethanol, and drying at 80 °C. The ternary nanocomposites were prepared by ultrasonication of calculated amounts of CC3 and WO_3 (as given in Table 1) in 50 mL of water for 3 h at room temperature. The precipitates were collected by centrifugation, washed with ethanol, and dried at 80 °C.

2.2 Characterization Techniques

The crystal structure of all the synthesized nanostructures ($CaWO_4$, WO_3, and g-C_3N_4) and the nanocomposites were studied by X-ray diffraction (XRD) using a Rigaku diffractometer. Optical absorption studies of the synthesized nanocomposites were carried out using a UV-2600 spectrophotometer. Nexus 470 was used to probe the vibrational modes of synthesized nanocomposites. The morphological studies and microstructural analysis were conducted using Field emission scanning electron microscopy (FESEM, JEOL, JEM-7001F) and high-resolution electron microscopy (HRTEM, JEOL JEM-2100F). Photocatalytic degradation efficiency of synthesized nanocomposites was measured using a lab-made photocatalytic reactor, and the decrease in dye concentration was monitored using a JASCO UV- Vis spectrophotometer.

2.3 Photocatalytic Experiment

Photocatalytic degradation of RhB was conducted using an indigenously constructed reactor. It consists of a 500 W halogen lamp and a double-walled glass container, both of which are separated at a distance of 15 cm. The dye solution and catalyst were taken in the double-walled container and stirred in the dark for the adsorption–desorption equilibrium. After attainment of equilibrium, the mixture (dye solution + catalyst) was irradiated with light, and the decrease in dye concentration was monitored at regular time intervals using a spectrophotometer. At any point in time, the percentage of dye degradation was calculated using the relation:

$$\%\ of\ dye\ degraded = \frac{C_0 - C_t}{C_0} \times 100 \quad \ldots (1)$$

where C_0 and C_t are the concentrations of dye at time "0" and "t" min, respectively.

Radical trapping experiments were conducted to identify the key species involved in the photodegradation process. The procedure was similar to that of the photodegradation experiments, except that radical scavengers were used along with the dye.

In the current study, photocatalytic degradation experiments were done in triplicate to ensure reproducibility. The degradation efficiencies and kinetic rate constants reported represent the average values of triplicate experiments, and the corresponding standard deviations were presented as error bars.

2.4 pH Drift Method

The point of zero charge (pHpzc) of the synthesized nanocomposites was found using the pH drift method (Jiao *et al.* 2017; Kosmulski, 2023). 50 mg of catalyst was suspended in the solutions of various pH levels prepared using NaOH and HCl. The suspension was stirred continuously, and the change in pH (ΔpH) was measured after 48 h. A graph was plotted by taking the initial pH on the X-axis and ΔpH on the Y-axis. The pH at which ΔpH = 0 is taken as pHpzc.

3. RESULTS AND DISCUSSION

3.1 X-ray Diffraction Studies

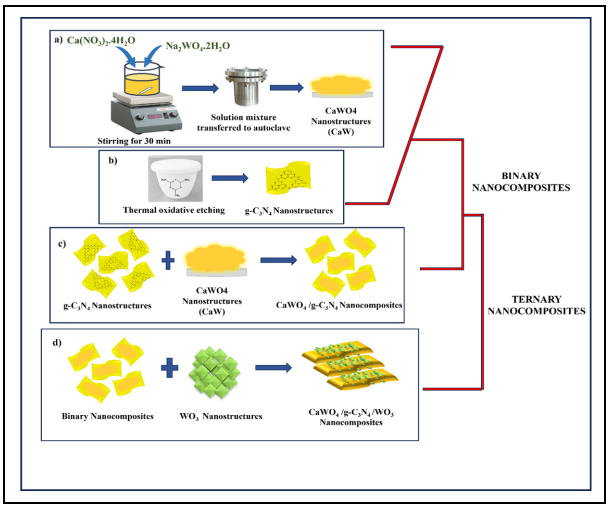


Fig. 1: Schematic representation of the synthesis of ternary nanocomposites

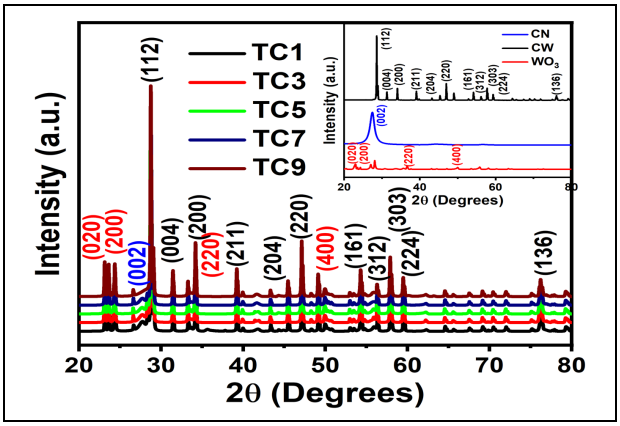


Fig. 2: X-ray diffraction patterns of $CaWO_4$/g-C_3N_4/WO_3 ternary nanocomposites [inset: XRD patterns of CN, CW, and WO_3]

Fig. 2 shows the X-ray diffraction patterns of ternary nanocomposites. The inset of Fig. 2 shows the XRD patterns of individual components of nanocomposites. The crystal structure and phase composition were analysed using XRD. The diffraction pattern of ternary nanocomposites exhibits peaks at 2θ = 28.8°, 31.4°, 34.1°, 39.2°, 43.3°, 47.7°, 54.2°, 56.3°, 57.9°, 59.7°, 76.3°, which correspond to (112), (004), (200), (211), (204), (220), (161), (312), (303), (224) and (136) planes of $CaWO_4$ (Scheelite phase, ICDD Card No. 01-085-0433), respectively (Yi and Jung, 2021). The peak at 2θ = 27.6° corresponds to the (002) plane of g-C_3N_4 with hexagonal phase (ICDD Card No. 01-87-1526) (Liu *et al*. 2011). The ternary composites exhibit peaks also at 2θ = 22.9°, 24.2°, 36.7°, and 50.1°, corresponding to (020), (200), (220), and (400) planes of hexagonal WO_3, respectively (Balzer *et al.* 2014; Boruah *et al.* 2020 and Liu *et al.* 2015). The synthesized compounds TC1, TC3, TC5, TC7, and TC9 exhibit diffraction patterns of three distinct compounds: $CaWO_4$, g-C_3N_4, and WO_3, which confirms their coexistence in the ternary nanocomposites. Further, the peak shift and broadening in ternary nanocomposites compared to distinct components indicate the localized structural deformation and strain caused by interaction between the components of nanocomposites (Alanazi and El Sayed, 2024; Li *et al.* 2022b).

The crystallite size (D) of the components was calculated using the Debye-Scherrer equation (Akhsassi *et al.* 2023):

$$D = \frac{k\lambda}{\beta cos\theta} \quad \ldots(2)$$

where, 'k' refers to the Scherrer constant, 'λ' is the wavelength of the X-ray used, β is the full width half maximum, and 'θ' is the diffraction angle. The analysis shows the crystallite size of the major component ($CaWO_4$) was 35 nm. Overall, the XRD analysis suggests the formation of ternary nanocomposites with very good interaction, and the absence of impurity peaks portrays the purity of the synthesized samples.

3.2 Optical Studies

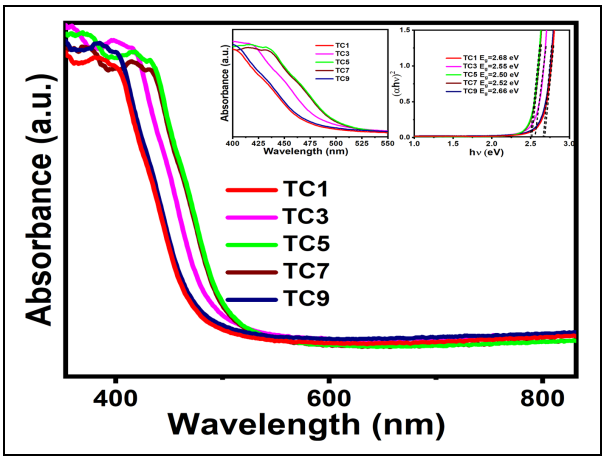


Fig. 3: UV–Vis DRS spectra of TC1, TC3, TC5, TC7, and TC9 ternary nanocomposites [inset: (a) enlarged UV–Vis DRS spectra showing a shift in absorbance and (b) Tauc plot]

The optical behaviour of ternary nanocomposites was studied using UV–Vis absorption spectroscopy and photoluminescence spectroscopy. This study aims to investigate the effect of WO_3 concentration on absorbance properties and charge carrier dynamics of synthesized nanocomposites. UV–Vis absorption spectra of ternary nanocomposites shown in Fig. 3 exhibit a distinct red shift in absorption edge with increasing the content of WO_3. The red shift is clearly visible in the enlarged UV–Vis absorption shown in inset 3(a). The ternary nanocomposites exhibit an absorption edge in the range of 470 to 500 nm, revealing the optical activation of catalysts by visible light. The ternary nanocomposites, TC5 and TC7, exhibit the highest red shift, with the absorbance edge around 475 nm.

The band gap of the nanocomposites was obtained from the Tauc plot using the relation:

$$\alpha h\nu = \left(h\nu - E_g\right)^n \quad \ldots(3)$$

where, 'α' is the coefficient of absorption, 'h' is the Planck's constant, 'ν' is the frequency of vibration, 'E_g' is the band gap of semiconductor and 'n' denotes the type of transition: n = 1/2 for direct transition and n = 2 for indirect transition (Akhsassi *et al.* 2024; Fritah *et al.* 2024). The Tauc plot [inset 3(b)] was constructed by plotting $h\nu$ on the x-axis and $(\alpha h\nu)^2$ on the y-axis. The band gap was obtained by extrapolating the linear portion of the graph to α = 0. The band gaps of TC1, TC3, TC5, TC7, and TC9 were 2.68, 2.55, 2.52, 2.50, and 2.66 eV, respectively. Among the synthesized ternary nanocomposites, TC5 and TC7 exhibit a greater

red shift with the lowest band gap of 2.50 and 2.52 eV, respectively. The reduction in band gap will help the nanocomposites to broaden their absorption spectrum, which makes it favourable for photocatalytic and optoelectronic applications (Sun *et al*. 2023).

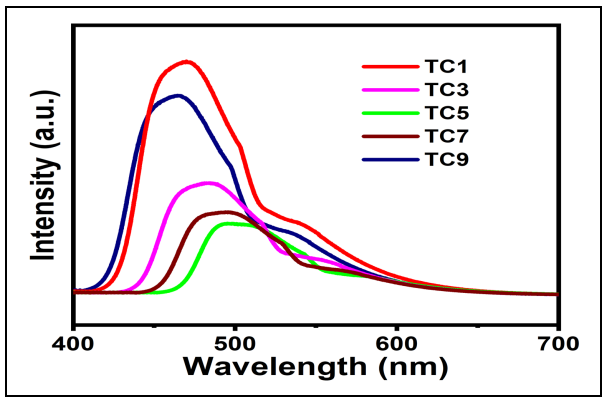


Fig. 4: Photoluminescence spectra of TC1, TC3, TC5, TC7, and TC9 ternary nanocomposites

Fig. 4 shows the photoluminescence spectra of ternary nanocomposites. It is clear that the emission wavelength and intensity of emission significantly change with WO_3 concentration in ternary nanocomposites. Among the synthesized ternary nanocomposites, TC5 exhibits the lowest PL intensity, portraying the improved separation and migration of charge carriers, which results in suppressed charge carrier recombination (Devi *et al*. 2024; Devi *et al.* 2023). Overall, the optical studies suggest that the concentration of WO_3 has influenced the band structure via better overlap of electronic orbitals and modifying the charge carrier dynamics of the nanocomposite materials.

3.3 Morphological Studies

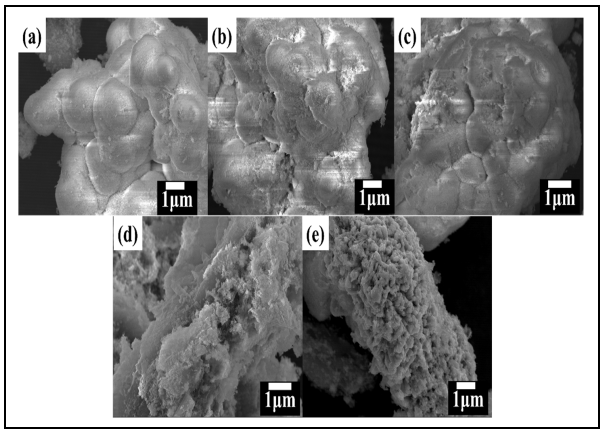


Fig. 5: (a–e) FESEM images of TC1, TC3, TC5, TC7, and TC9 ternary nanocomposites

The morphology and microstructure of ternary nanocomposites were studied using FESEM and TEM analysis. Fig 5(a–e) displays the FESEM images of ternary nanocomposites with 1, 3, 5, 7, and 9% WO_3, respectively. The micrographs of TC1, TC3, and TC5 [Fig. 5(a–c)] exhibit nanostructures with quasi-spherical morphology. The binary ($CaWO_4$/g-C_3N_4) nanocomposites, reported in a previous work (Vadivu *et al.* 2025), showed the uniform distribution of $CaWO_4$ over g-C_3N_4 nanostructures, which are loose and fluffy quasi-spherical nanostructures. In the present work, the addition of WO_3 to the binary nanocomposite (CC3) has not disturbed the distribution, and the ternary nanocomposites below 5% WO_3 resulted in a similar morphology, which is evident from the better distribution of WO_3, resulting in efficient heterojunction formation. However, at higher WO_3 (TC7 and TC9) concentration, the agglomeration between the particles is greater, resulting in a less porous, denser surface morphology. This might be due to the overloading of WO_3 in ternary nanocomposites. The denser morphology will have less open surface, in which the active sites will hinder and may suppress the photocatalytic performance of the nanocomposites (Liu *et al.* 2022; Vavilapalli *et al.* 2024). The microstructure changes (TC1–TC5) demonstrate a smooth and homogeneous anchoring of the WO_3 nanoparticles on the surfaces of $CaWO_4$/g-C_3N_4 at lower concentrations of WO_3, as appropriate dispersion was achieved with ultrasonic mixing, along with superior interface contact for charge transport across the heterojunction. On the contrary, at a higher gathering of WO_3 denoting clusters (TC7 and TC9), charge mobility was reduced as the available surface area active was reduced from particle collisions and overt nucleation, which can block available reaction sites. The reductions in light penetration and charge mobility account for a reduction in the photocatalytic efficiency observed at the higher concentrations of WO_3.These microstructure variations confirm that WO_3 plays a crucial role in determining interface contact and charge mobility. The optimal morphology achieved at 5% WO_3 (TC5) promotes efficient heterojunction formation, whereas excessive WO_3 content causes agglomeration that inhibits surface activity and suppresses photocatalytic efficiency.

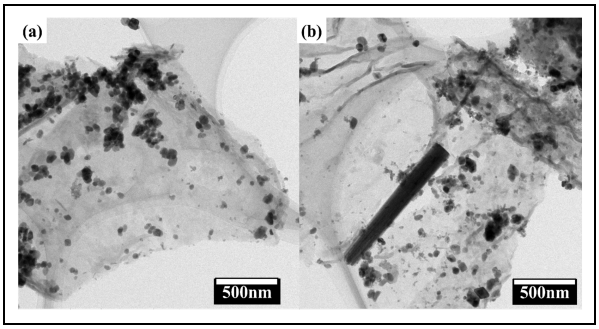


Fig. 6: TEM images of (a) TC1 and (b) TC5 ternary nanocomposites, showing internal morphology and interfacial contact between the components

Further insight into the nanostructures was obtained from TEM images, which are displayed in Fig. 6. The TEM images of nanocomposites, TC1 [Fig. 6(a)] and TC5 [Fig. 6(b)], display well-defined contact between the components of the nanocomposites, resulting in a tightly coupled heterostructure. The nanocomposites with well-dispersed components and strong structural configuration will support the efficient charge separation and suppress its recombination, which is vital for photocatalytic applications (Bonde *et al.* 2024; Melinte *et al*. 2019, and Rokesh *et al.* 2021).

The morphological studies are comparable with the observations obtained from the optical studies. The morphological studies reveal that the nanocomposites are more aggregated at higher WO_3 concentration. Similarly, the intensity of PL emission for TC7 is increased compared to TC5. Furthermore, the XRD patterns confirm the formation of nanocomposites without affecting the crystalline phases of individual components. Hence, comparing the structural, optical, compositional, and morphological analysis, it is understood that the synergistic effects of components of nanocomposites at optimal concentration modulate the electronic structure and facilitate better overlap of orbitals, robust heterojunction, and superior charge carrier dynamics to make it a promising candidate for photocatalytic applications. Overall, the microstructural evolution observed with varying WO_3 concentration demonstrates that processing parameters critically govern interfacial density, porosity, and particle connectivity. The optimized TC5 composition achieves a balance between uniform dispersion and heterojunction integrity, whereas excessive WO_3 loading induces agglomeration and surface densification, which negatively affects charge transport and surface reactivity. This microstructure–performance correlation explains the observed photocatalytic trend.

3.4 Textural Analysis

Table 2. BET surface area, total pore volume, average pore diameter, and BET C constant of the ternary nanocomposites with different WO_3 loadings (TC1, TC5, and TC9) obtained from N_2 adsorption–desorption measurements

Sample	BET Surface Area (m^2/g^{-1})	Total Pore Volume (cm^3g^{-1})	Average Pore Diameter (nm)	BET C Constant
TC1	14.02	0.1238	17.66	91.55
TC5	11.25	0.1509	26.84	288.05
TC9	1.09	0.1097	201.7	30.14

The surface area, pore volume, and pore structure of the ternary nanocomposites with three different loadings of WO_3 (TC1, TC5, and TC9), using N_2 adsorption–desorption measurements, are presented in Table 2.

The BET surface area of TC1 (1% WO_3) was the largest, measuring 14.02 $m^2\ g^{-1}$; however, the most beneficial pore structure was in TC5 (5% WO_3 + 3% g-C_3N_4), having a total pore volume of 0.1509 $cm^3\ g^{-1}$ and a mesoporous average pore diameter of 26.84 nm. The high C value of TC5, at 288.05, supports that the adsorbate–surface interaction is much stronger, indicating its surface is more heterogeneous, and active sites are more accessible.

The larger mesopores in TC5 facilitate:

- The diffusion of RhB molecules into the interior of the catalyst,
- improved light penetration due to reduced scattering and,
- enhanced adsorption and trapping of dye molecules prior to degradation.

Relative to TC1 and TC5 samples, TC9 (9% WO_3) had a very low surface area of 1.09 $m^2\ g^{-1}$ and an unusually large pore size of ~200 nm due to the agglomeration of excessive WO_3, which blocked active sites and shielded both $CaWO_4$ and g-C_3N_4 surfaces from visible-light. These data reinforce that TC5 represents the optimal loading for achieving a synergistic mesoporous structure, which enhances reactant diffusion and electron-transfer pathways, thereby improving photocatalytic degradation of RhB.

3.5 Compositional Studies

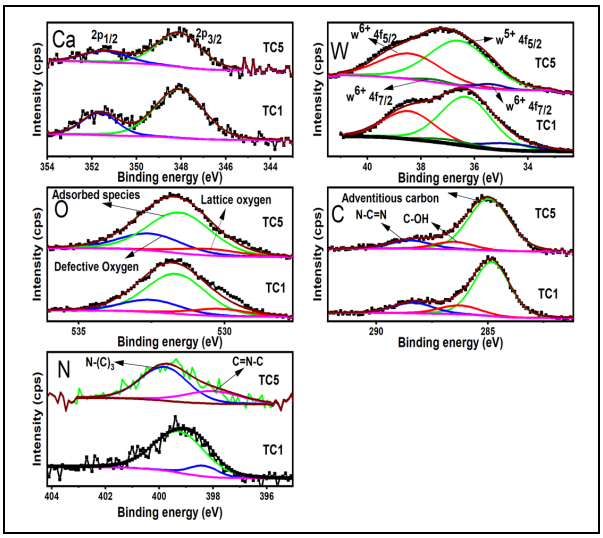


Fig. 7: High-resolution XPS spectra of Ca, W, O, N, and C for TC1 and TC5 nanocomposites, confirming the chemical states of the constituent elements

The surface chemical composition and electronic interactions within the nanocomposites can be studied using XPS. Fig. 7 shows the high-resolution spectra of Ca, W, O, N, and C for both TC1 and TC5 nanocomposites. High-resolution spectrum of Ca 2p exhibits two prominent peaks corresponding to Ca 2p1/2 and Ca 2p3/2 of Ca^{2+} in $CaWO_4$. Further, no significant peak shift is observed between TC1 and TC5, signifying a stable chemical state of Ca^{2+} (Yadav *et al*. 2023). The high-resolution W 4f spectra of TC1 and TC5 are deconvoluted into two doublets corresponding to W^{6+} and W^{5+} oxidation states. Doublet at higher binding energies (38.6 and 37.4 eV) corresponds to 4f5/2 and 4f7/2W^{6+} oxidation state. The doublet at lower binding energies (36.3 and 34.5 eV) corresponds to 4f5/2 and 4f7/2W^{5+} oxidation state (Ganbavle *et al.* 2014). The quantitative analysis of the W^{6+}: W^{5+} ratio is approximately 4:7 for TC1 and 1:2 for TC5, suggesting a higher proportion of W^{5+} in TC5. The increase in W^{5+} suggests the formation of a greater density of oxygen vacancies and defect sites. Further, the peaks of TC5 are shifted slightly, which might be the result of improved electronic interaction between the components $CaWO_4$, g-C_3N_4, and WO_3. The presence of such improved electronic interaction will facilitate the charge-separation process and thus increase the photocatalytic efficiency of nanocomposites (Al-Harthi *et al.* 2025).

The high-resolution O 1s spectra exhibit peaks around 530 eV, 531.5 eV, and 533 eV, corresponding to lattice oxygen, defective oxygen, and adsorbed oxygen species (Lim *et al.* 2023). The TC5 shows a higher contribution of adsorbed oxygen, which can contribute to the enhancement of photocatalytic performance via improved surface reactivity of nanocomposites.TC1 and TC5 exhibit two nitrogen peaks centered approximately at 398.5 eV [C=N-C] and 400.2 eV [N-$(C)^3$], which are the usual peaks observed in g-C_3N_4. Similarly, the peaks of adventitious carbon (~284.6), C-OH (~286.1 eV), and N-C=N (288.4 eV) are displayed in C 1s high-resolution spectra. On the whole, the results of XPS suggest a stronger interaction between the components of nanocomposites, which aids the better charge transfer and heterojunction formation in TC5.

The FTIR spectra are presented in Fig. 8. All the ternary nanocomposites exhibit a strong band around 400–800 cm^{-1}, which can be attributed to metal-oxygen bonds: Ca–O and W–O stretching vibrations (Mohammadi, 2017; Najafi-Ashtiani *et al.* 2018). The presence of the above distinct bands supports the formation of a metal oxide network. The characteristic peaks of g-C_3N_4 appeared in the 1200 to 1700 cm^{-1} range. The peaks at 1215 cm^{-1} and 1317 cm^{-1} are attributed to the stretching vibration of C-NH-C (Sunasee *et al.* 2019). The stretching vibrations of C–N appeared at 1398 cm^{-1}, 1535 cm^{-1}, and 1633 cm^{-1}. The broad absorption band from 3500 to 3000 cm^{-1} corresponds to O–H stretching modes (Sunasee *et al.* 2019). The presence of Ca–O, W–O, and g-C_3N_4 peaks confirms the presence of $CaWO_4$, g-C_3N_4, and WO_3 in ternary nanocomposites.

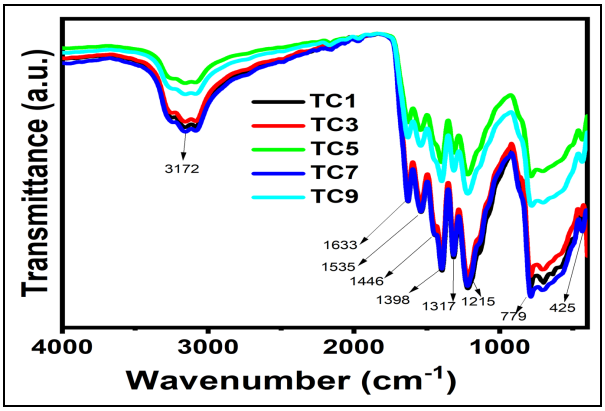


Fig. 8: FTIR spectra of TC1, TC3, TC5, TC7, and TC9 ternary nanocomposites, showing the characteristic functional groups of the components

3.6 Optimization of Photocatalytic Performance

Photocatalytic degradation of organic compounds is a complex interplay that consists of a series of physical and chemical phenomena, including surface interactions (adsorption/desorption), diffusion of incident light into the medium and its subsequent absorption by the catalyst, charge separation, and charge transfer dynamics. To understand these physical and chemical phenomena, photocatalytic degradation of RhB by TC5 was investigated using various reaction parameters like catalyst dosage, dye concentration, and pH of dye solution.

Catalyst dosage is a key parameter that significantly affects the photocatalytic degradation, as it determines the active sites and generation of reactive oxygen species. In a photocatalytic reaction, an optimal level of catalyst will improve photon absorption and charge carrier generation. However, beyond the optimal amount, detrimental effects were observed (Ahmaruzzaman and Mishra, 2021; Arulkumar *et al.* 2023). In the current study, the effect of photocatalyst dosage is studied by varying the TC5 amount between 20 and 100 mg/L, and the results are displayed in Fig. 9(a). It is evident from Fig. 9(a) that the degradation of RhB increases as the catalyst amount is increased from 20 to 80 mg/L. The addition of a catalyst below the optimal level increases the active sites and enhances the ROS generation. However, beyond 80 mg/L, light scattering increases, light penetration decreases, and thus reduces the generation of charge carriers, finally reducing the photocatalytic performance of the catalyst (Ahmaruzzaman and Mishra, 2021; Yekta *et al.* 2016). Thus, 80 mg/L is taken as the optimal level of photocatalyst.

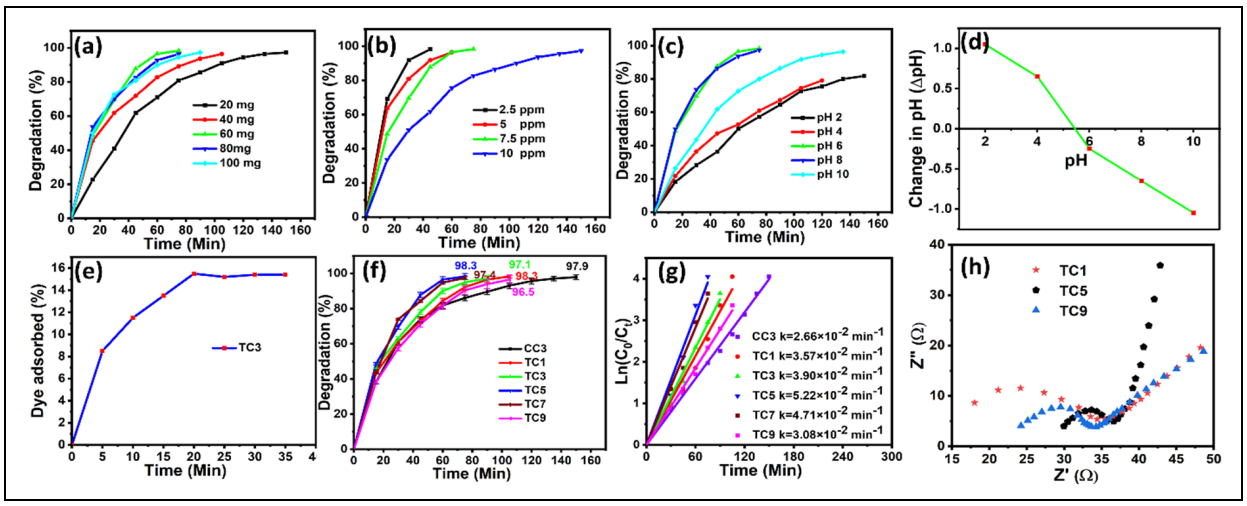


Fig. 9: Optimization and photocatalytic performance of ternary nanocomposites for RhB degradation under visible-light irradiation: (a) effect of catalyst dosage, (b) effect of dye concentration, (c) effect of pH, (d) pH drift method, (e) adsorption of the dye under dark conditions, (f) photocatalytic activity of the synthesized nanocomposites, (g) kinetics of RhB degradation, and (h) EIS spectra

The effect of initial dye concentration on photocatalytic degradation efficiency of TC5 was examined by varying the RhB concentration from 2.5 ppm to 10 ppm [Fig. 9(b)]. The degradation efficiency of the catalyst exhibits an inverse relationship with dye concentration. Further, at higher concentration (10 ppm), the efficiency of the catalyst falls drastically. The dye at higher concentration shields the catalyst's surface and decreases the photons reaching the catalyst surface, which results in decreased photocatalytic performance (Magar *et al.* 2022). Hence, from systematic analysis, 7.5 ppm is taken as the optimum RhB concentration, achieving 98% degradation in 75 min.

The effect of pH on the photocatalytic performance of TC5 is studied over pH values from 2 to 10 [Fig. 9(c)]. The maximum degradation efficiency 98% in 150 min is achieved at pH = 8. This is because the catalyst exhibits pHpzc at 6.8, determined using the pH drift method (Fig. 9(d)) (Askari *et al.* 2020; El Aouni *et al.* 2024). Hence, the catalyst exhibits a positively charged surface below pH 6.8 and a negatively charged surface above its pHpzc. In this scenario, the RhB, being a cationic dye, gets adsorbed over the catalyst surface more effectively at pH greater than pHpzc. At pH = 8, there is a favourable electrostatic interaction between the surface of TC5 and RhB dye, which subsequently enhances the photocatalytic activity (Laatar *et al.* 2017; Yuan *et al.* 2023). However, at very high pH, the presence of a higher amount of OH– will act as a scavenger and thus reduce the photocatalytic efficiency of TC5.

The adsorption of dye under dark conditions is evaluated by stirring 7.5 ppm of dye along with 80 mg/L of catalyst at pH = 8. Absorbance of dye solution in the dark is measured at regular intervals and presented in Fig. 9(e). The absorbance of the dye solution becomes constant after 15 min, showing the establishment of adsorption–desorption equilibrium in a short time. Thus, the studies reveal the importance of light for the degradation of the RhB dye solution.

Fig. 9(f) shows the systematic evaluation of the photocatalytic performance of binary (CC3) and ternary nanocomposites against RhB as a model pollutant. The incorporation of WO_3 to $CaWO_4$/g-C_3N_4 in varying ratios caused a notable change in the photocatalytic performance of the synthesized ternary nanocomposites. Among the variants, TC5 exhibited the highest photocatalytic activity, degrading 98% of RhB dye in 75 min, under visible light irradiation. This remarkable achievement can be attributed to the formation of an efficient ternary heterojunction, which can promote the charge carrier separation and suppress the recombination of charge carriers, thereby increasing the availability of reactive species required for the photodegradation process. Further, the optimal concentration of WO_3 in TC5 creates well-aligned band structures that facilitate the interfacial charge transfer and improve redox efficiency during photocatalysis. In contrast, lower concentration of WO_3 (TC1 and TC3 may not provide sufficient interfacial contact, whereas higher concentration of WO_3 (TC7 and TC9) may induce agglomeration or excess charge trapping, which could act as recombination centers, thereby reducing the overall photocatalytic efficiency.

To further understand the photocatalytic process, kinetic studies were performed by applying a pseudo-first-order kinetic model, which is appropriate for dilute dye concentrations where the surface coverage of the photocatalyst remains constant. This relationship can be expressed as:

$$ln\left(\frac{C_0}{C_t}\right) = kt \quad \ldots (4)$$

where, C_0 and C_t are the initial and instantaneous concentration of RhB at time t, and k is the apparent rate constant. The linear plots of $\ln(C_0/C_t)$ vs. time [Fig. 9(g)] for all samples indicated that the degradation followed pseudo-first-order kinetics. Each experiment was performed in triplicate, and error bars representing the standard deviations have been included in the kinetic plots to demonstrate reproducibility. The rate constant k for TC5 (5.40×10^{-2} min^{-1}) is significantly higher than those of CC3 (2.69×10^{-2} min^{-1}) and other ternary nanocomposites, portraying its superior degradation rate. This is consistent with the enhanced charge separation and synergistic interactions among $CaWO_4$, g-C_3N_4, and WO_3 in TC5, which collectively promote efficient generation of reactive species such as hydroxyl radicals (HO•) and superoxide radicals (O_2^-•), leading to rapid RhB degradation. Thus, both the degradation efficiency and kinetic analysis unambiguously demonstrate that TC5 exhibits the best photocatalytic behaviour among all the tested nanocomposites.

Fig. 9(h) shows the Nyquist impedance plots of TC1 in the high-frequency region. Each of the catalysts exhibits a distinct semicircular arc, which corresponds to the charge transfer process at the interface of the semiconductor and electrolyte. Among the three samples, TC5 exhibits a smaller arc diameter, signifying the lowest charge transfer resistance, resulting in the highest level of interfacial electron transport and the least recombination of photogenerated charge carriers. This is attributed to the unique effects of the band alignment of $CaWO_4$, g-C_3N_4, and WO_3 in the TC5 ternary nanocomposite, which enhances its ability to transport electrons across the heterojunction interface. In contrast, TC1 and TC9 both have larger semicircle diameters, indicating that interfacial kinetics could potentially be slower. The trend of the R_{ct} values (TC5 < TC9 < TC1) was directly related to the photocatalytic performance, indicating that the increase in charge separation and mobility in TC5 was responsible for the further degradation of RhB.

A clearer understanding of the structure–property relationship can be obtained by correlating the crystalline phases with charge carrier behaviour. The enhanced photocatalytic activity of TC5 is associated with its crystalline structure and balanced heterojunction interface. The scheelite $CaWO_4$ crystal structure gives a robust host lattice for efficient charge transport channels, and the π-conjugated structure of g-C_3N_4 allows efficient electron transfer and transport through its extended electronic structure. The introduction of WO_3 creates defect sites, increases oxygen vacancies, improves the charge trapping ability, and enhances visible light absorption. The unique combination of excellent crystallinity, coherent lattice contact, and interfacial electric field effectively improves the separation and transfer of these charge carriers to promote improved photocatalytic activity. This demonstrates that structural organization and interfacial engineering can have a significant impact on the photocatalytic activity of the ternary nanocomposites.

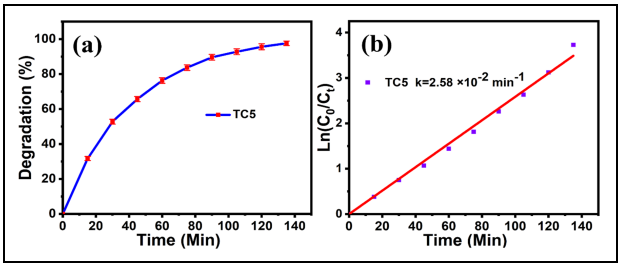


Fig. 10: (a) photocatalytic activity and (b) kinetic study of TC5 nanocomposites for the photocatalytic degradation of RhB under natural sunlight

The practical feasibility of a photocatalyst is strongly influenced by its long-term stability and reusability under repeated use. To evaluate this practical feasibility, the photodegradation of RhB was studied using TC5 for repeated cycles, and the results were presented in Fig. 10(a). After each cycle, the photocatalyst is recovered by centrifugation, washed with distilled water and ethanol to remove residual dye and byproducts, and then dried at 70 °C before reuse in the subsequent cycle.

In the first cycle, TC5 achieved a RhB degradation efficiency of approximately 98%, and in the fifth cycle, 94% RhB degradation was observed. Further, the structural stability of the optimized photocatalyst (TC5) was examined using XRD studies, as shown in Fig. 10(b). The positions and relative intensities of the diffraction peaks that correspond to $CaWO_4$, g-C_3N_4, and WO_3 were unchanged compared to the fresh catalyst, indicating that the ternary nanocomposite-maintained phase stability and chemical integrity throughout its use. No other reflections corresponding to impurities or secondary phases were observed, indicating that the material did not decompose or undergo any phase transitions during the photocatalytic process.

There was a slight decrease in overall peak intensities and some reflections (specifically, the (112) and (211) planes of calcium tungstate) broadened slightly upon reuse, which is likely due to surface fouling by the dye intermediates or microstrain development as well as some partial amorphization of the outer surface layer (Sádaba *et al.* 2015). The Scherrer crystallite size of the (112) peak changed from ~35.2 nm (fresh) to ~33.8 nm (after reuse), which corresponds to a change of less than 5%. This demonstrates the excellent structural stability of TC5

during photocatalysis. It is evident that the enhanced photocatalytic performance of TC5 originates not from a single factor, but from the combined influence of optimized processing conditions, favorable crystalline structure, controlled microstructure evolution, and efficient interfacial charge-transfer pathways.

The persistence of all characteristic peaks along with a very small increase in crystallite size and absence of new phases showed that the CaWO4/g-C_3N_4/WO_3 heterostructure is very stable and reusable, which matches well with the minor decrease in efficiency of degradation of RhB (98% to 94% after five cycles).

3.7 Radical Scavenging and Solar Photocatalytic Activity

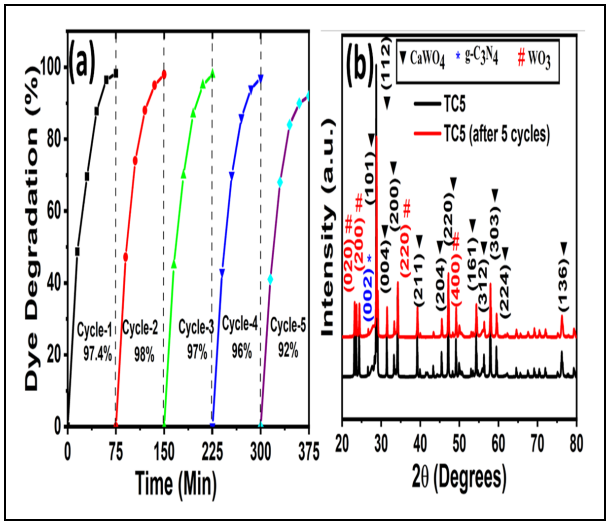


Fig. 11: (a) reusability study of TC5 nanocomposites for photocatalytic degradation of RhB and (b) XRD patterns of TC5 before and after five photocatalytic cycles

To elucidate the dominant reactive species involved in the photocatalytic degradation of RhB by TC5 nanocomposite, radical scavenger experiments were carried out under visible light irradiation, as depicted in Fig. 11. In this study, disodium salt of ethylenediaminetetraacetic acid (EDTA-Na), isopropyl alcohol (IPA) and benzoquinone (BQ) are used as scavengers for hole (h^+), hydroxyl radical (HO•) and superoxide radicals (O_2^-•), respectively.

The photocatalytic performance of TC5 in the absence of any scavenger exhibited the highest RhB degradation efficiency, indicating efficient generation and participation of reactive oxygen species. However, introducing specific scavengers, BQ and IPA, significantly reduced the degradation efficiency, indicating the effective participation of hydroxyl radical (HO•) and superoxide radicals (O_2^-•) in the degradation of RhB by TC5. Nevertheless, the introduction of EDTA-Na has not reduced the photocatalytic performance to a greater extent, suggesting lesser involvement of holes (h^+) in RhB degradation. These results strongly imply that the hydroxyl radical (HO•) and superoxide radicals (O_2^-•) are primary oxidative species responsible for RhB degradation, whereas photogenerated holes (h^+) play a secondary role in RhB degradation.

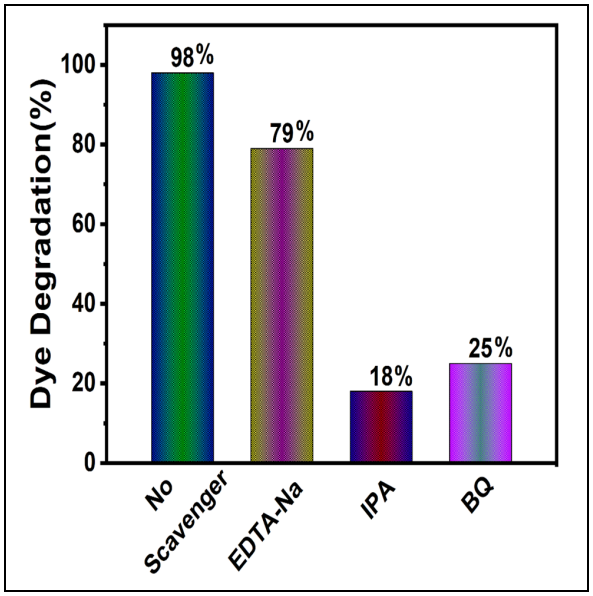


Fig. 12: Radical scavenging experiments identifying the dominant reactive species involved in RhB degradation

The photocatalytic activity of the optimized nanocomposite (TC5) was also evaluated using natural sunlight to test its practical applications. Fig. 12 shows the photocatalytic activity and kinetics of TC5 against RhB under direct sunlight. Under solar irradiation, TC5 achieved nearly complete (~97%) decoloration of RhB dye within 135 min, showcasing its outstanding, solar-driven photocatalytic activity. The reaction kinetics followed a pseudo-first-order model with a rate constant, $k = 2.58 \times 10^{-2}$ min^{-1}, although the degradation rate constant under solar light was slightly lower than that observed under artificial visible-light irradiation ($k = 5.22 \times 10^{-2}$ min^{-1}). This difference is attributed to the lower and variable light intensity and the broader spectral distribution of natural sunlight.

This suggests that the $CaWO_4$/g-C_3N_4/WO_3 ternary heterojunction demonstrates effective utilization of visible light and charge carrier separation under broad-spectrum solar light. The enhancement in photocatalytic activity can be attributed to the multiple semiconductors acting synergistically in an S-scheme configuration, facilitating electron transfer and the generation of ROS.

Table 3. Comparison of RhB photodegradation performance of $CaWO_4/g\text{-}C_3N_4/WO_3$ (TC5) ternary nanocomposite with previously reported photocatalysts under different light sources

Catalyst	Light Source	Time (min)	Degradation (%)	Rate constant, k (min^{-1})	Reference
CdS QDs/La-Bi_2WO_6	Xenon lamp	70	99	Not mentioned	Ning *et al.* 2023
$Bi_2S_3/g\text{-}C_3N_4$	Natural sunlight	120	90	0.73×10^{-2}	Basely *et al.* 2023
$g\text{-}C_3N_4/NiFe_2O_4$	Natural sunlight	60	99	2.7×10^{-2}	Mishra *et al.* 2024
FeS_2/TiO_2	Solar radiation	180	97	2.01×10^{-2}	Alsulmi *et al.* 2024
$Ag_2CO_3/g\text{-}C_3N_4$	Natural sunlight	120	95	1.41×10^{-2}	Alsulmi *et al.* 2023
$AgI/g\text{-}C_3N_4$	Visible-light	120	92	1.9×10^{-2}	Alsulmi *et al.* 2024b
$\alpha\text{-}Fe_2O_3/g\text{-}C_3N_4/SiO_2$	Visible-light	120	97	2.38×10^{-2}	Sharma *et al.* 2023
GQDs/BiOBr	xenon lamp	140	83	4.4×10^{-2}	Liu *et al.* 2024
$SnS_2/g\text{-}C_3N_4$	Solar radiation	120	96	Not mentioned	Alsalme *et al.* 2024
$ZnFe_2O_4/Ag_3PO_4/ZnIn_2S_4$	Solar radiation	150	100	2.1×10^{-2}	Kumar *et al.* 2024*
Ternary $CdS/TiO_2/g\text{-}C_3N_4$	visible light	180	99	2.7×10^{-2}	Shoaib *et al.* 2023*
$BiOCl/BiOBr/SnS_2$	Visible	20	96	14.33×10^{-2}	Liu *et al.* 2024*
CdSQDs@ZnS/ZnO	Under simulated sunlight	120	91	Not mentioned	Cao *et al.* 2026*
$ZnIn_2S_4/BiOCl/FeVO_4$	Visible light	30	98	Not mentioned	Kumar *et al.* 2023*
Ag_3PO_4 /$CoWO_4$ /$g\text{-}C_3N_4$	Visible light	90	90	2.4×10^{-2}	Aishwarya *et al.* 2026*
$CaWO_4/g\text{-}C_3N_4/WO_3$	Halogen lamp	75	98	5.40×10^{-2}	Present work
$CaWO_4/g\text{-}C_3N_4/WO_3$	Natural sunlight	135	97	2.58×10^{-2}	Present work

***double-S-scheme mechanism**

To validate the efficiency of the optimized photocatalyst (TC5), its RhB degradation performance was compared with that of recently reported photocatalysts under different light irradiation (Table 3). TC5 exhibits remarkably high degradation efficiency of 98% in 75 min with a rate constant of 5.40×10^{-2} min^{-1}, which is higher than the reported catalysts. The photocatalytic performance of TC5 even under sunlight is substantially higher than most of the reported systems.

The superior photocatalytic activity of TC5 can be attributed to:

- the well-aligned double S-scheme heterojunction, which enhances charge separation and suppresses recombination
- the presence of mesoporous architecture, which eases the mass transfer, and
- the optimal WO_3 loading that enables efficient band alignment without inducing agglomeration.

These results suggest that the photocatalytic performance of TC5 is comparable to that of several reported ternary systems. Thus, the study validates the practical feasibility of TC5 for real wastewater remediation. The catalyst retained 94% degradation efficiency after five consecutive cycles, demonstrating excellent structural durability and operational reliability for long-term use. The photocatalytic performance of TC5 under natural sunlight confirms its potential applicability in solar-driven wastewater treatment systems, offering the advantage of reduced energy consumption. The high activity, stability, and reusability indicate that the $CaWO_4/g\text{-}C_3N_4/WO_3$ ternary nanocomposite can be considered a promising and scalable photocatalyst for practical industrial and environmental purification processes.

3.8 Mechanism

The probable mechanism, band edge potentials, and charge carrier mobility of the synthesized nanocomposite are shown in Fig. 13. The synergistic interaction between the components of the

nanocomposites results in enhanced photocatalytic performance. The band edge potentials of $CaWO_4$, g-C_3N_4, and WO_3 were calculated using the empirical formula (Luo *et al*. 2018, 2017):

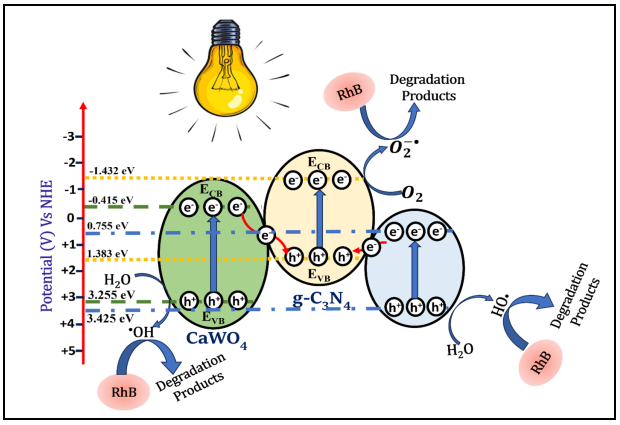


Fig. 13: Schematic illustration of band-edge potentials, charge transfer and reactions in $CaWO_4$ /g-C_3N_4/WO_3 nanocomposites

$$E_{CB} = \chi - E_e - \frac{1}{2}E_g \quad \ldots (5)$$

$$E_{VB} = E_{CB} + E_g \quad \ldots (6)$$

where E_{VB} and E_{CB} are the conduction band and valence edge potential of the semiconductor, χ is the Mulliken electronegativity, calculated by taking the arithmetic mean of atomic electron affinity and first ionization energy, E_e is the free-electron energy on the hydrogen (NHE) scale, and E_g is the band gap of the semiconductor. The band gap obtained from the Tauc plot and the calculated band edge potential are presented in Table 4.

Table 4. Mulliken electronegativity, electron free energy, band gap, and band-edge potentials of $CaWO_4$, g-C_3N_4, and WO_3 nanostructures

Compound	χ (eV)	E^e	E_g	E_{cb}	E_{vb}
$CaWO_4$	5.92 (Bilgin Simsek and Tuna, 2024)	4.5	3.67	-0.415	3.255
g-C_3N_4	4.483 (Praus, 2021)	4.5	2.83	-1.432	1.398
WO_3	6.59 (Székely *et al.* 2021)	4.5	2.67	0.755	3.425

Based on the optical studies and band edge potentials presented in Table 3, a double S-scheme heterojunction is proposed for $CaWO_4$/g-C_3N_4/WO_3 nanocomposites. When the nanostructures at optimum ratio are mixed/prepared together under suitable conditions, they will interact with each other to form nanocomposites with efficient heterojunction, resulting in better optical properties and improved photocatalytic activity (Wei *et al.* 2022). In the current work, TC5 exhibits better light absorption and suppressed PL emission, and hence, it is expected to have good interaction between the components. Further, TC5 exhibits the smallest semicircular arc, which signifies the lowest interfacial charge-transfer resistance with efficient electron migration. Under such conditions, the interfacial charge redistribution effect will drive the flow of electrons easily from WO_3 to g-C_3N_4 as well as from $CaWO_4$ to g-C_3N_4 until the Fermi levels reach equilibrium, which is accompanied by the creation of a strong internal electric field at the interface and bending of band edges.

The alignment of the Fermi levels of $CaWO_4$, g-C_3N_4, and WO_3 creates an internal electric field, which governs the motion of photogenerated charge carriers. When light excites electrons in the valence band of these semiconductors, electron-hole pairs (e-h) are generated through the excitation of electrons to the conduction band. In the S-scheme mechanism, electrons in the conduction bands of $CaWO_4$ and WO_3 recombine with the holes in the valence band of g-C_3N_4 at the heterojunction interface. This recombination process eliminates low-energy charge carriers while retaining highly reactive electrons in the conduction band of g-C_3N_4 and holes in the valence bands of $CaWO_4$ and WO_3. The retained conduction band electrons, which possess strong reduction potential, reduce dissolved oxygen to form superoxide radicals, while the retained holes with high oxidation potential generate hydroxyl radicals from water. The charge transfer pathway created by this process leads to the recycling of e-h pairs that suppresses recombination, thus resulting in significantly enhanced redox activity and a measurable enhancement of photocatalytic degradation efficiency.

During the process of photocatalytic activity, when the nanocomposites are irradiated with the light of a suitable wavelength, photogenerated charge carriers are formed within the components of the nanocomposites. Due to interfacial band bending, electrons from $CaWO_4$ and WO_3 recombine with holes in g-C_3N_4, while the remaining charge carriers with strong redox ability actively participate in RhB degradation. The photogenerated electrons in g-C_3N_4 combine with O_2 to form superoxide radical ion($O_2^{-\bullet}$), whereas the holes in WO_3 and $CaWO_4$ react with water to form hydroxyl radical (HO•). The reactive species thus formed subsequently degrade the RhB dye. Thus, the formation, transfer and utilization of the charge carriers in the ternary nanocomposite system can be visualized as given in Fig. 13. Also, the proposed mechanistic pathway is in line with the results of radical scavenging activity, which portrays the superoxide radical ion ($O_2^{-\bullet}$) and hydroxyl radical (HO•) as primary reactive species in RhB photodegradation by ternary nanocomposites. The mechanistic interpretation presented in this study is derived from a comprehensive

correlation of complementary structural, optical, electrochemical, and photocatalytic analyses; advanced *in-situ* or *operando* characterizations, though valuable, are beyond the scope of the present study.

The intermediates of RhB degradation using TC5 under visible light can be studied using Liquid Chromatography–Mass Spectrometry (LC–MS). The reaction mixture collected after 120 min of photocatalysis (by TC5) was subjected to LC–MS analysis after removing the catalyst by centrifugation. The chromatogram exhibits peaks at m/z = 443, 415, 387, 359, 331, 303, 275, 247, 219, and 191 at different retention times. Among these, the peak at m/z = 443 corresponds to RhB, whereas peaks at m/z = 415 and 387 are commonly assigned to intermediates like mono- and di-N-deethylated RhB. The successive deethylation and partial oxidation of the xanthene core is established by peaks at m/z = 359 and 331. Further, the lower mass peaks at m/z = 303, 275, 247, 219, and 191 are the result of ring opening and progressive oxidative breakdown of the conjugated backbone, to form small carboxylic acids. The assignment of intermediates is based on comparison of m/z values with previously reported LC–MS fragmentation data. These intermediates confirm that the RhB photodegradation process using ternary nanocomposites proceeds via sequential N-deethylation followed by oxidative cleavage toward mineralization.

4. CONCLUSION

A series of $CaWO_4/g\text{-}C_3N_4/WO_3$ ternary nanocomposites was synthesized and systematically assessed for their structural integrity, optical properties, and photocatalytic activity. Structural confirmation and coexistence of individual components were confirmed by XRD and FTIR. The light absorption characteristics as well as charge carrier dynamics of ternary nanocomposites were investigated by UV-Vis absorption and PL studies, which revealed that TC5 exhibited enhanced absorption and efficient charge transfer. Among the ternary nanocomposites, TC5 exhibits the best photocatalytic performance with 98% RhB degradation within 75 min under visible light irradiation, with a rate constant of 5.40×10^{-2} min^{-1}, owing to its optimal band alignment and robust heterojunction interface. Kinetic analysis followed pseudo-first-order behaviour, and radical scavenging tests revealed HO• and O_2^{-}• as the primary reactive species.

Further, the TC5 ternary nanocomposite showed remarkable stability, retaining about 94% degradation efficiency after five consecutive photocatalytic cycles, indicating excellent structural durability and reusability. Under natural sunlight irradiation, the catalyst achieved nearly 97% degradation of RhB within 135 min, demonstrating its effective solar-driven photocatalytic performance. Overall, this study demonstrates that rational control of processing parameters and interfacial engineering, even without complex post-synthesis modifications, can yield highly efficient $CaWO_4/g\text{-}C_3N_4/WO_3$ ternary photocatalysts for visible-light-driven wastewater remediation and scalable environmental applications.

FUNDING

This research received no specific grant from any funding agency in the public, commercial, or not-for-profit sectors.

CONFLICTS OF INTEREST

The authors declare that there is no conflict of interest.

COPYRIGHT

This article is an open-access article distributed under the terms and conditions of the Creative Commons Attribution (CC BY) license (http://creativecommons.org/licenses/by/4.0/).

REFERENCES

Ahmaruzzaman, M. and Mishra, S. R., Photocatalytic performance of g-C_3N_4 based nanocomposites for effective degradation/removal of dyes from water and wastewater, *Mater. Res. Bull.,* 143, 111417 (2021). https://doi.org/10.1016/j.materresbull.2021.111417

Aishwarya, A., Chowdhury, A. P., Anantharaju, K. S., Vidya, Y. S. and Gurushantha, K., Dual S-scheme $Ag_3PO_4/CoWO_4/g\text{-}C_3N_4$ ternary nanocomposite for photo degradation of Rhodamine B pollutant and electrochemical detection of acetaminophen, *J. Water Process Eng.,* 82, 109421 (2026). https://doi.org/10.1016/j.jwpe.2025.109421

Akhsassi, B., Bouddouch, A., Naciri, Y., Ettahiri, Y., Bakiz, B., Taoufyq, A., Villain, S., Guinneton, F., Gavarri, J. R. and Benlhachemi, A., Visible light-driven type II p-Bi_3O_4Cl/n-$BiPO_4$ heterojunction for effective photocatalytic photodegradation, *Ceram. Int.,* 50(18), 32338–32352 (2024). https://doi.org/10.1016/j.ceramint.2024.06.041

Akhsassi, B., Naciri, Y., Bouddouch, A., Bakiz, B., Taoufyq, A., Villain, S., Favotto, C., Valmalette, J. C., Gavarri, J. R. and Benlhachemi, A., Facile novel acid coprecipitation synthesis of $BiPO_4$ polymorphs: Enhanced photocatalytic degradation of the antibiotic AMX and the dyes RhB, MB and MO, *Opt. Mater.,* 137, 113575 (2023). https://doi.org/10.1016/j.optmat.2023.113575

Alanazi, T. I. and El Sayed, A. M., Structural, optical analysis, stress-strain, and dielectric properties of selenium oxide/$LaFeO_3$/blend nanocomposites with tunable properties for optoelectronics and micro-supercapacitors, *J. Energy Storage,* 95, 112652 (2024). https://doi.org/10.1016/j.est.2024.112652

Al-Harthi, E. A., Imran, M., Rashid, M. S., Asghar, A., Khan, H. R., Shakera, M. A., Yakout, A. A. and Khan, A., Enhanced charge transfer kinetics in high-performance CeO_2-TiO_2 nanocomposites for hybrid asymmetric supercapacitor, *Inorg. Chem. Commun*., 178, 114616 (2025). https://doi.org/10.1016/j.inoche.2025.114616

Alsalme, A., Hesham, M., Soltan, A., Mohammed, N. N., Nejm, A. Q., Messih, M. F. A., Hussein, I. A. and Ahmed, M. A., Pioneering the design of S-scheme SnS_2/g-C_3N_4 nanocomposites via sonochemical and physical mixing methods for solar degradation of cationic rhodamine B dye, *Mater. Adv.,* 5(18), 7278–7295 (2024). https://doi.org/10.1039/D4MA00718B

Alsulmi, A., Mohammed, N. N., Shaker, M. H., Basely, A. M., Abdel, -M. M. F., Eltawil, A. M., sultan, A. and Ahmed, M. A., Rational Design of Magnetic Recyclable S-Scheme FeS_2/TiO_2 Heterojunction for Photocatalytic Degradation of Rhodamine B dye Under Broad Solar Spectrum, *J. Inorg. Organomet. Polym. Mater.,* 34(4), 1628–1642 (2024a). https://doi.org/10.1007/s10904-023-02904-5

Alsulmi, A., Hussein, I. A., Nasherty, M., Hesham, M., Soltan, A., Messih, M. F. A. and Ahmed, M. A., Sonochemical Fabrication of S-Scheme AgI/g-C_3N_4 Heterojunction for Efficient Photocatalytic Degradation of RhB Dye*, J. Inorg. Organomet. Polym. Mater.,* 34(2), 640–654 (2024b). https://doi.org/10.1007/s10904-023-02854-y

Alsulmi, A., Shaker, M. H., Basely, A. M., Abdel, -M. M. F., Sultan, A. and Ahmed, M. A., Engineering S-scheme Ag_2CO_3/g-C_3N_4 heterojunctions sonochemically to eradicate Rhodamine B dye under solar irradiation, *RSC Adv*., 13, 12229–12243 (2023). https://doi.org/10.1039/D3RA00173C

Arulkumar, E., Shree, S. S. and Thanikaikarasan, S., Photocatalytic degradation efficiency of Rhodamine B for CuO/CdO nanosheets attained through simple co-precipitation method, *Results Chem*., 6, 101169 (2023). https://doi.org/10.1016/j.rechem.2023.101169

Askari, N., Beheshti, M., Mowla, D. and Farhadian, M., Synthesis of $CuWO_4$/Bi_2S_3 Z-scheme heterojunction with enhanced cephalexin photodegradation, *J. Photochem. Photobiol. A Chem.,* 394, 112463 (2020). https://doi.org/10.1016/j.jphotochem.2020.112463

Balakrishnan, A. and Chinthala, M., Comprehensive review on advanced reusability of g-C_3N_4 based photocatalysts for the removal of organic pollutants, *Chemosphere,* 297, 134190 (2022). https://doi.org/10.1016/j.chemosphere.2022.134190

Balzer, R., Drago, V., Schreinerc, W. H. and Probsta, L. F. D., Synthesis and structure-activity relationship of a WO_3 catalyst for the total oxidation of BTX, *J. Braz. Chem. Soc.,* 25, 2026–2031 (2014). https://doi.org/10.5935/0103-5053.20140187

Basely, A. M., Shaker, M. H., Helmy, F. M., Abdel, -M. M. F. and Ahmed, M. A., Construction of Bi_2S_3/g-C_3N_4 step S-scheme heterojunctions for photothermal decomposition of rhodamine B dye under natural sunlight radiations, *Inorg. Chem. Commun.,* 148, 110300 (2023). https://doi.org/10.1016/j.inoche.2022.110300

Bilgin, S. E. and Tuna, Ö., Understanding the nature of Ce–Fe synergy in the structure $CaWO_4$ scheelite for enhanced photocatalytic performance under visible light, *Ceram. Int.,* 50(11), 20600–20611 (2024). https://doi.org/10.1016/j.ceramint.2024.03.181

Bonde, S., Kallawar, G., Bhanvase, B. A. and Sathe, B., Nanocomposites and their applications in photocatalytic degradation processes, *Photocatal. Energy Environ. Sustainability,* 4, 1-49 (2024). https://doi.org/10.1088/978-0-7503-5697-8ch4

Boruah, P. J., Khanikar, R. R. and Bailung, H., Synthesis and Characterization of Oxygen Vacancy Induced Narrow Bandgap Tungsten Oxide (WO_3−x) Nanoparticles by Plasma Discharge in Liquid and Its Photocatalytic Activity, *Plasma Chem. Plasma Process.,* 40, 1019–1036 (2020). https://doi.org/10.1007/s11090-020-10073-3

Cao, Z., Zhang, C., Jiang, S., Liu, H., Yu, Y. and Li, L., Bifunctional CdSQDs@ZnS/ZnO composites with double S-scheme heterojunctions and oxygen-rich vacancies for enhanced photocatalysis, *New J. Chem.,* 50(7), 3037–3051 (2026). https://doi.org/10.1039/d5nj04012d

Devi, S., Kumar, S., Devi, J., Sharma, A. and Kumar, A., Decoration of 1,3 oxazole modified g-C_3N_4 by Bio-synthesized Ag nanoparticle for the photodegradation of pharmaceutical effluent: Clotrimazole, *Mater. Today Proc.,* (2023). https://doi.org/10.1016/j.matpr.2023.03.630

Devi, S., Kumari, S., Sharma, A., Dhiman, M., Thakur, M. and Kumar, A., Boosting the photocatalytic activity of g-C_3N_4 via loading bio-synthesized Ag0 nanoparticles and imidazole modification for the degradation and mineralization of fluconazole, *Environ. Sci. Pollut. Res.,* 31, 15851–15871 (2024). https://doi.org/10.1007/s11356-024-31834-z

Dutta, V., Sharma, S., Raizada, P., Thakur, V. K., Khan, A. A. P., Saini, V., Asiri, A. M. and Singh, P., An overview on WO_3 based photocatalyst for environmental remediation, *J. Environ. Chem. Eng.,* 9(1), 105018 (2021). https://doi.org/10.1016/j.jece.2020.105018

El Aouni, A., El Ouardi, M., Arab, M., Saadi, M., Haspel, H., Kónya, Z., Ben Ali, A., Jada, A., BaQais, A. and Ait Ahsaine, H., Design of Bismuth Tungstate Bi_2WO_6 Photocatalyst for Enhanced and Environmentally Friendly Organic Pollutant Degradation, *Mater.,* 17(5), 1029 (2024). https://doi.org/10.3390/ma17051029

Feijoo, S., Kamali, M. and Dewil, R., A review of wastewater treatment technologies for the degradation of pharmaceutically active compounds: Carbamazepine as a case study, *Chem. Eng. J.*, 455, 140589 (2023). https://doi.org/10.1016/j.cej.2022.140589

Fritah, K., Khachane, M., Bouddouch, A., Akhsassi, B., Bakiz, B., Taoufyq, A., El Aamrani, A. and Benlhachemi, A., New insight for enhanced photocatalytic activity of Bi4-xLaxTi3O12 ($0 \leq x \leq 1$) solid solution: A case study on degradation of Rhodamine B under UV light irradiation, *Opt. Mater.,* 150, 115182 (2024). https://doi.org/10.1016/j.optmat.2024.115182

Ganbavle, V. V., Agawane, G. L., Moholkar, A. V., Kim, J. H. and Rajpure, K. Y., Structural, optical, electrical, and dielectric properties of the spray-deposited WO_3 thin films, *J. Mater. Eng. Perform.*, 23, 1204–1213 (2014). https://doi.org/10.1007/s11665-014-0873-3

Gumma, S., Prasad, P. R., Punyasamudram, S., Sreedevi, A., Putta, V. N. K. and Kanuparthy, P. R., In Situ Synthesis of $ZnCo_2O_4$ and $Pd@ZnCo_2O_4$ Nanocomposites for Dye Degradation and Biological Applications, *J. Environ. Nanotechnol.,* 13(3), 41–51 (2024). https://doi.org/10.13074/jent.2024.09.242735

Jabbar, Z. H., Graimed, B. H., Ammar, S. H., Sabit, D. A., Najim, A. A., Radeef, A. Y. and Taher, A. G., The latest progress in the design and application of semiconductor photocatalysis systems for degradation of environmental pollutants in wastewater: Mechanism insight and theoretical calculations, *Mater. Sci. Semicond. Process.,* 173, 108153 (2024). https://doi.org/10.1016/j.mssp.2024.108153

Jiao, Y., Han, D., Lu, Y., Rong, Y., Fang, L., Liu, Y. and Han, R., Characterization of pine-sawdust pyrolytic char activated by phosphoric acid through microwave irradiation and adsorption property toward CDNB in batch mode, *Desalin. Water Treat.*, 77, 247–255 (2017). https://doi.org/10.5004/dwt.2017.20780

Kato, S. and Kansha, Y., Comprehensive review of industrial wastewater treatment techniques, *Environ. Sci. Pollut. Res.,* 31(39), 51064–51097 (2024). https://doi.org/10.1007/s11356-024-34584-0

Kosmulski, M., The pH dependent surface charging and points of zero charge. X. Update, *Adv. Colloid Interface Sci.,* 319, 102973 (2023). https://doi.org/10.1016/j.cis.2023.102973

Kumar, Y., Sonu, Sudhaik, A., Raizada, P., Nguyen, V. H., Kumar, N., Kaya, S., Ahamad, T., Hussain, C. M. and Singh, P., Fabrication of novel ternary dual S-scheme $ZnFe_2O_4/Ag_3PO_4/ZnIn_2S_4$ photocatalyst with enhanced visible light-driven RhB degradation, *J. Ind. Eng. Chem.,* 138, 543–554 (2024). https://doi.org/10.1016/j.jiec.2024.04.032

Kumar, Y., Sudhaik, A., Sharma, K., Sonu, Raizada, P., Khan, P. A. A., Nguyen, V. H., Ahamad, T., Singh, P. and Asiri, A. M., Construction of magnetically separable novel arrow down dual S-scheme $ZnIn_2S_4/BiOCl/FeVO_4$ heterojunction for improved photocatalytic activity, *J. Photochem. Photobiol. A Chem.,* 435, 114326 (2023). https://doi.org/10.1016/j.jphotochem.2022.114326

Laatar, F., Moussa, H., Alem, H., Balan, L., Girot, E., Medjahdi, G., Ezzaouia, H. and Schneider, R., CdSe nanorod/TiO_2 nanoparticle heterojunctions with enhanced solar- and visible-light photocatalytic activity, *Beilstein J. Nanotechnol.*, 8, 2741–2752 (2017). https://doi.org/10.3762/bjnano.8.273

Li, R. L., Thrasher, C. J., Hueckel, T. and Macfarlane, R. J., Hierarchically Structured Nanocomposites via a "systems Materials Science" Approach, *Acc. Mater. Res.,* 3(12), 1248–1259 (2022a). https://doi.org/10.1021/accountsmr.2c00153

Li, X., Chen, Y., Tao, Y., Shen, L., Xu, Z., Bian, Z. and Li, H., Challenges of photocatalysis and their coping strategies, *Chem Catalysis*, 2(6), 1315–1345 (2022b). https://doi.org/10.1016/j.checat.2022.04.007

Lim, T., Jo, K. and Lee, H., Oxygen Vacancy and Valence Band Structure of $Ba0.5Sr0.5Fe1-xCuxO3-\delta$ ($x = 0–0.15$) with Enhanced ORR Activity for IT-SOFCs, *Mater.*, 16(8), 3231 (2023). https://doi.org/10.3390/ma16083231

Liu, C., Qin, Y., Guo, W., Shi, Y., Wang, Z., Yu, Y. and Wu, L., Visible-light-driven photocatalysis over nano-TiO_2 with different morphologies: From morphology through active site to photocatalytic performance, *Appl. Surf. Sci.,* 580, 152262 (2022). https://doi.org/10.1016/j.apsusc.2021.152262

Liu, F., Chen, X., Xia, Q., Tian, L. and Chen, X., Ultrathin tungsten oxide nanowires: oleylamine assisted nonhydrolytic growth, oxygen vacancies and good photocatalytic properties, *RSC Adv.*, 5(94), 77423–77428 (2015). https://doi.org/10.1039/c5ra12993a

Liu, J., Zhang, T., Wang, Z., Dawson, G. and Chen, W., Simple pyrolysis of urea into graphitic carbon nitride with recyclable adsorption and photocatalytic activity, *J. Mater. Chem.,* 21(38), 14398–14401 (2011). https://doi.org/10.1039/c1jm12620b

Liu, Y., Zhang, X., Li, X. and Zhou, Z., Visible light driven S-scheme GQDs/BiOBr heterojunction with enhanced photocatalytic degradation of Rhodamine B and mechanism insight, *J. Water Process Eng*., 57, 104588 (2024). https://doi.org/10.1016/j.jwpe.2023.104588

Luo, J., Zhou, X., Ning, X., Zhan, L., Huang, L., Cai, Q., Li, S. and Sun, S., Enhancing visible-light photocatalytic performance and stability of Ag_3PO_4 nanoparticles by coupling with hierarchical flower-like In_2S_3 microspheres, *Mater. Res. Bull.,* 100, 102–110 (2018). https://doi.org/10.1016/j.materresbull.2017.12.012

Luo, J., Zhou, X., Ning, X., Zhan, L., Ma, L., Xu, X., Huang, Z. and Liang, J., Synthesis and characterization of Z-scheme In_2S_3/Ag_2CrO_4 composites with an enhanced visible-light photocatalytic performance, *New J. Chem.,* 41(2), 845–856 (2017). https://doi.org/10.1039/C6NJ02934E

Magar, M. H., Adole, V. A., Waghchaure, R. H. and Pawar, T. B., Efficient photocatalytic degradation of eosin blue dye and antibacterial study using nanostructured zinc oxide and nickel modified zinc oxide, *Results Chem*., 4, 100537 (2022). https://doi.org/10.1016/j.rechem.2022.100537

Matesun, J., Petrik, L., Musvoto, E., Ayinde, W. and Ikumi, D., Limitations of wastewater treatment plants in removing trace anthropogenic biomarkers and future directions: A review, *Ecotoxicol. Environ. Saf.,* 281, 116610 (2024). https://doi.org/10.1016/j.ecoenv.2024.116610

Maurera, M. A. M. A., Souza, A. G., Soledade, L. E. B., Pontes, F. M., Longo, E., Leite, E. R. and Varela, J. A., Microstructural and optical characterization of $CaWO_4$ and $SrWO_4$ thin films prepared by a chemical solution method, *Mater. Lett.,* 58(5), 727–732 (2004). https://doi.org/10.1016/j.matlet.2003.07.002

Melinte, V., Stroea, L. and Chibac, -S. A. L., Polymer Nanocomposites for Photocatalytic Applications, *Catal.,* 9(12), 986 (2019). https://doi.org/10.3390/catal9120986

Mishra, S., Acharya, L., Sharmila, S., Sanjay, K. and Acharya, R., Designing g-C_3N_4/$NiFe_2O_4$ S-scheme heterojunctions for efficient photocatalytic degradation of Rhodamine B and tetracycline hydrochloride, *Appl. Surf. Sci. Adv*., 24, 100647 (2024). https://doi.org/10.1016/j.apsadv.2024.100647

Mohamadpour, F. and Amani, A. M., Photocatalytic systems: reactions, mechanism, and applications, *RSC Adv.,* 14(29), 20609–20645 (2024). https://doi.org/10.1039/D4RA03259D

Mohammadi, -A. S., Green synthesis and characterization of Pr^{3+}:$CaWO_4$ nanostructures in the presence of maltose as a capping agent for photocatalytic degradation of rhodamine B, *J. Mater. Sci. Mater. Electron.,* 28, 17161–17167 (2017). https://doi.org/10.1007/s10854-017-7644-5

Murillo, -S. J. C., Hernández, -R. A., Hinojosa, -R. L. and Guzmán, -M. J. L., A review on the development of visible light-responsive WO_3-based photocatalysts for environmental applications, *Chem. Eng. J. Adv.,* 5, 100070 (2021). https://doi.org/10.1016/j.ceja.2020.100070

Najafi, -A. H., Bahari, A., Gholipour, S. and Hoseinzadeh, S., Structural, optical and electrical properties of WO_3–Ag nanocomposites for the electro-optical devices, *Appl. Phys. A.,* 124, 24 (2018). https://doi.org/10.1007/s00339-017-1412-5

Ning, J., Zhang, B., Siqin, L., Liu, G., Wu, Q., Xue, S., Shao, T., Zhang, F., Zhang, W. and Liu, X., Designing advanced S-scheme CdS QDs/La-Bi_2WO_6 photocatalysts for efficient degradation of RhB, *Exploration,* 3(5), 20230050 (2023). https://doi.org/10.1002/exp.20230050

Niu, P., Zhang, L., Liu, G. and Cheng, H. M., Graphene-like carbon nitride nanosheets for improved photocatalytic activities, *Adv. Funct. Mater.,* 22(22), 4763–4770 (2012). https://doi.org/10.1002/adfm.201200922

Praus, P., On electronegativity of graphitic carbon nitride, *Carbon*, 172, 729–732 (2021). https://doi.org/10.1016/j.carbon.2020.10.074

Rokesh, K., Sakar, M. and Do, T. O., Emerging Hybrid Nanocomposite Photocatalysts for the Degradation of Antibiotics: Insights into Their Designs and Mechanisms, *Nanomateri.,* 11(3), 572 (2021). https://doi.org/10.3390/nano11030572

Sádaba, I., Granados, L. M., Riisager, A. and Taarning, E., Deactivation of solid catalysts in liquid media: the case of leaching of active sites in biomass conversion reactions, *Green Chem.,* 17(8), 4133–4145 (2015). https://doi.org/10.1039/C5GC00804B

Samuel, O., Othman, M. H. D., Kamaludin, R., Sinsamphanh, O., Abdullah, H., Puteh, M. H. and Kurniawan, T. A., WO_3–based photocatalysts: A review on synthesis, performance enhancement and photocatalytic memory for environmental applications, *Ceram. Int.,* 48(5), 5845–5875 (2022). https://doi.org/10.1016/j.ceramint.2021.11.158

Sharma, K., Sudhaik, A., Raizada, P., Thakur, P., Pham, X. M., Le, V. Q., Nguyen, V. H., Ahamad, T., Thakur, S. and Singh, P., Constructing alpha-Fe_2O_3/g-C_3N_4/SiO_2 S-scheme-based heterostructure for photo-Fenton like degradation of rhodamine B dye in aqueous solution, *Environ. Sci. Pollut. Res.,* 30, 124902–124920 (2023). https://doi.org/10.1007/s11356-022-24940-3

Shoaib, M., Naz, M. Y., Shukrullah, S., Munir, M. A., Irfan, M., Rahman, S. and Ghanim, A. A. J., Dual S-Scheme Heterojunction $CdS/TiO_2/g\text{-}C_3N_4$ Photocatalyst for Hydrogen Production and Dye Degradation Applications, *ACS Omega,* 8, 43139–43150 (2023). https://doi.org/10.1021/acsomega.3c06759

Shobana, T., Venkatesan, T., Saravanan, S. S. R., Kathirvel, D. and Valliyammal, K., Facile Synthesis and Characterization of Pure and Bi-doped ZnS Nanoparticles for Photocatalytic Application, *J. Environ. Nanotechnol.,* 13(3), 108–114 (2024). https://doi.org/10.13074/jent.2024.09.243870

Singh, B. J., Chakraborty, A. and Sehgal, R., A systematic review of industrial wastewater management: Evaluating challenges and enablers, *J. Environ. Manage*., 348, 119230 (2023). https://doi.org/10.1016/j.jenvman.2023.119230

Singhal, M., Jangir, S., Upadhyay, S. and Rajawat, D. S., Advances in graphitic carbon nitride: a comprehensive review of synthesis, properties, applications and recent developments with photoelectrochemical water splitting, *Discover Chem.,* 1, 64 (2024). https://doi.org/10.1007/s44371-024-00055-1

Sun, Y., Zhang, W., Li, Q., Liu, H. and Wang, X., Preparations and applications of zinc oxide based photocatalytic materials, *Adv. Sens. Energy Mater*., 2(3), 100069 (2023). https://doi.org/10.1016/j.asems.2023.100069

Sunasee, S., Leong, K. H., Wong, K. T., Lee, G., Pichiah, S., Nah, I. W., Jeon, B. H., Yoon, Y. and Jang, M., Sonophotocatalytic degradation of bisphenol A and its intermediates with graphitic carbon nitride, *Environ. Sci. Pollut. Res.,* 26, 1082–1093 (2019). https://doi.org/10.1007/s11356-017-8729-7

Székely, I., Kedves, E. Z., Pap, Z. and Baia, M., Synthesis design of electronegativity dependent WO_3 and $WO_3{\cdot}0.33H_2O$ materials for a better understanding of TiO_2/WO_3 composites' photocatalytic activity, *Catal.,* 11(7), 779 (2021). https://doi.org/10.3390/catal11070779

Tahir, M. B., Sagir, M., Zubair, M., Rafique, M., Abbas, I., Shakil, M., Khan, I., Afsheen, S., Hasan, A. and Ahmed, A., WO_3 Nanostructures-Based Photocatalyst Approach Towards Degradation of RhB Dye, *J. Inorg. Organomet. Polym. Mater.,* 28, 1107–1113 (2018). https://doi.org/10.1007/s10904-017-0771-x

Vadivu, A., Venkatachalam, M. and Silambarasan, A., Assessment of the photocatalytic activity of scheelite $CaWO_4/g\text{-}C_3N_4$ nanocomposites via rhodamine B degradation under visible light, *Transition Met. Chem.,* 50, 609-624 (2025). https://doi.org/10.1007/s11243-025-00644-8

Vavilapalli, D. S., Qin, L., Palisaitis, J. and Rosen, J., Enhanced photocatalytic performance of a rGO-$Ca_2Fe_2O_5$ nanocomposite for photodegradation of emergent pollutants, *NPJ Clean Water,* 7, 41 (2024). https://doi.org/10.1038/s41545-024-00334-5

Wei, X., Yi, H., Lai, C., Huo, X., Ma, D. and Du, C., Synergistic effect of flower-like $MnFe_2O_4/MoS_2$ on photo-Fenton oxidation remediation of tetracycline polluted water, *J. Colloid Interface Sci.,* 608, 942–953 (2022). https://doi.org/10.1016/j.jcis.2021.10.033

Yadav, B., Kar, K. K., Ghorai, M. K. and Kumar, D., Exploring the dielectric and conduction characteristics of iodine substituted $CaCu_3Ti_4O_{12}$-xIx, *Ceram. Int.,* 49(4), 6932–6945 (2023). https://doi.org/10.1016/j.ceramint.2022.10.289

Yekta, S., Sadeghi, M. and Babanezhad, E., Synthesis of $CaWO_4$ nanoparticles and its application for the adsorption-degradation of organophosphorus cyanophos, *J. Water Process Eng*., 14, 19–27 (2016). https://doi.org/10.1016/j.jwpe.2016.10.004

Yi, S. S. and Jung, J. Y., Calcium Tungstate Doped with Rare Earth Ions Synthesized at Low Temperatures for Photoactive Composite and Anti-Counterfeiting Applications, *Crystals,* 11(10), 1214 (2021). https://doi.org/10.3390/cryst11101214

Yuan, C., Sun, F., Liu, H., Chen, T., Chu, Z., Wang, H., Zou, X., Zhai, P. and Chen, D., Synthesis of $CaWO_4$ as a Photocatalyst for Degradation of Methylene Blue and Carmine under Ultraviolet Light Irradiation, *Processes,* 11(4), 1050 (2023). https://doi.org/10.3390/pr11041050